



OPEN

# Improving the structural, optical, and electrical properties of carboxymethyl cellulose/starch/selenium oxide nanocomposites for flexible electronic devices

Adel M. El Sayed<sup>1✉</sup> & Tarek I. Alanazi<sup>2✉</sup>

Nanocomposites based on biopolymers are interesting materials owing to their multifunctionality and ease of preparation. In this study, the solution casting method was used to mix selenium oxide nanoparticles (SeO<sub>2</sub> NP) made by a solvothermal method into a bio-blend of carboxymethyl cellulose and starch (CMC/St). XRD analysis showed that SeO<sub>2</sub> NP increased the amorphous portion inside the blend. HR-TEM revealed the spherical morphology of these NP with an average diameter of 16.88 nm. The FE-SEM indicated a satisfactory uniform distribution and homogeneity in the surface morphology of the films. FTIR confirmed the interaction between SeO<sub>2</sub> and the blend functional groups. The films preserved good transmission after doping, and their direct and indirect band gaps decreased. The refractive index, absorption index, optical conductivity, and other dispersion parameters were improved after SeO<sub>2</sub> loading. The DC conductivity of the blend is in the range of  $3.8 \times 10^{-7}$  to  $5.6 \times 10^{-4}$  S/m and improved after loading SeO<sub>2</sub> NP. The IV characteristic curves in the temperature range of 300–415 K were studied to figure out the conduction mechanism in the CMC/St/SeO<sub>2</sub> composites. Because the optical and electrical properties improved, these nanocomposites could be used for coatings and other things like waveguides, photovoltaic cells, and light-emitting diodes.

The increasing need for eco-friendly multifunctional polymeric materials arises from some concerns related to environmental preservation and technological progress. Combining two or more biocompatible polymers in a blend that combines the advantages of the individual polymers can partially satisfy these requirements. The blending approach yields novel materials that could be used in a wider range of products and applications, such as UV absorbers, sensors, membranes, radiation shields, microelectronic devices, food packaging, and drug delivery systems. The properties of the blend can also be improved by adding nano-sized materials to the blend matrix. This is called polymeric nanocomposite formation<sup>1–4</sup>. The chitin/cashew gum blend had better thermal and mechanical properties than the single polymers. Adding 10% wt% Fe<sub>3</sub>O<sub>4</sub> NP to the mix made it ideal for magnetic shielding materials and actuators<sup>5</sup>. Adding nanochitosan to polyvinyl alcohol (PVA) and cashew gum improved the semiconducting and dielectric properties of the blend and made it suitable for capacitors and flexible energy storage applications<sup>6</sup>. A nanocomposite made of carboxymethyl chitosan/cashew gum matrix loaded with boehmite NP was used by Meera and Ramesan<sup>7</sup> for charge harvesting devices and flexible electronics. The material at the nanoscale displays unique physicochemical features in comparison with its bulk counterparts. This is owing to the high surface area and quantum confinement effects<sup>8,9</sup>.

Two of the most easily obtained polymers from renewable resources are cellulose and its CMC derivative, known as CMC or sodium salt. CMC is hydrophilic, semi-crystalline, has good film-forming ability and physiological inactivity, is biodegradable, and is nontoxic. Besides, it has good thickening, viscosity, stabilizing, and binding abilities and can produce flexible and strong films by blending with proteins<sup>2,10,11</sup>. These features make CMC suitable for various uses in medicine, pharmacy, agriculture, industry, and several products such as lotions, creams, and toothpaste. However, despite these advantages, some limitations to using CMC alone exist. Blending CMC with other polymers can mitigate these problems. Salem et al.<sup>2</sup> found that adding polypyrrole enhanced the

<sup>1</sup>Physics Department, Faculty of Science, Fayoum University, El-Fayoum 63514, Egypt. <sup>2</sup>Department of Physics, College of Science, Northern Border University, 73222 Arar, Saudi Arabia. ✉email: ams06@fayoum.edu.eg; tarek.alanazi@nbu.edu.sa

thermal stability of CMC but achieved optical conductivity on only  $10^{11} \text{ S}^{-1}$ . Another biodegradable, abundant, and non-toxic polymer is starch (St). This material consists of linear amylose and amylopectin that are clustered and branched<sup>12</sup>. Like CMC, it is widely used for food and non-food utilization, including paper and textiles, wound dressings, and drug carriers. Cheap CMC/St hydrogels with high water uptake were prepared by gamma irradiation for superabsorbent polyelectrolytes<sup>13</sup>. According to El Miri et al.<sup>14</sup>, adding cellulose nanocrystals (0.5–5.0 wt%) to the CMC/St blend improved its viscoelastic and mechanical properties. The bio-nanocomposites that were made are good for use in packaging. There was research by Sun et al.<sup>15</sup> that looked at how sodium alginate, starch, xanthan gum, gelatin, propanetriol, sorbitol, PEG400, and PEG 6000 changed the thermal and mechanical properties of carboxymethyl bacterial cellulose. A suitable thermal stability was achieved when 1.0% sodium alginate and 0.2% propanetriol were added.

$\text{SeO}_2$  is a photosensitive semiconductor that is a promising material for photosensors, photovoltaics, and photoelectrochemical applications<sup>16,17</sup>. The solvothermally prepared  $\text{SeO}_2$  nanorods were used as a nanoadditive and a catalyst and were found to be able to make the diesel oil hotter and more volatile<sup>18</sup>. On the other hand, a selenium-free diet leads to liver malfunction and immune and neural system dysfunction<sup>19</sup>. The daily intake of Se for humans should be in the range of 60–70 mg. Some bacteria can't form biofilms on  $\text{SeO}_2$  NP<sup>20</sup>. It can also kill microbes and cancer cells and break down the methylene blue dye when exposed to visible light. Therefore,  $\text{SeO}_2$  is useful for water treatment, antifungal drugs, and other interesting fields<sup>21,22</sup>.

A few reports on the preparation, optical, and AC electrical properties of polymer/ $\text{SeO}_2$  are found in the literature. Some researchers<sup>1,3</sup> studied the antibacterial activity of a  $\text{SeO}_2$ -doped PVP/CMC blend. They also found that adding 0.8 wt%  $\text{SeO}_2$  made the blend more conductive, going from  $6.45 \times 10^{-7} \text{ S/cm}$  to  $2.24 \times 10^{-6} \text{ S/cm}$  at room temperature (RT)<sup>3</sup>. The effect of  $\text{SeO}_2$  NP and Se/Ag amounts on the optical and dielectric properties of chitosan/polyacrylamide (PAAm) was also reported<sup>16,23,24</sup>. To the best of the author's knowledge, no report on CMC/St/ $\text{SeO}_2$  bio-nanocomposites has been found. This work is devoted to leveraging the physicochemical properties of CMC, St and nanosized  $\text{SeO}_2$  and studying the structure, morphology, and optical properties of the prepared CMC/St/ $\text{SeO}_2$  nanocomposites. Moreover, the IV characteristic, DC conductivity, and conduction mechanism are discussed.

## Experimental section

### Chemicals and preparation

Selenium (Se) powder and  $\text{NaBH}_4$  (sodium borohydride) as a capping agent were supplied by Sigma Aldrich. Starch powder of molecular weight 260,000 g/mol and chemical formula  $(\text{C}_6\text{H}_{10}\text{O}_5)_n$ , was supplied by Advent Chembio Pvt. Ltd (India). CMC powder  $(\text{C}_8\text{H}_{15}\text{NaO}_8)_n$  of molecular weight 90,000 g/mol, was supplied by El-Nasr Co., (Egypt). Double-distilled (DD) water was used as a common solvent. 0.1 M of Se and 7.5 M of  $\text{NaBH}_4$  were dissolved in 35 mL DD water using a magnetic stirrer at RT. The color of Se turned into a black precipitate after 2 h of stirring. Then the solution was transferred into an autoclave (100 mL) and processed at 175 °C for one day. The precipitate (selenium hydroxides) was then filtered and washed five times with DD water, ethanol, and methanol. Finally, the powder was heat-dried at 100–110 °C in an air furnace and annealed at 400 °C in an Ar atmosphere for 2 h. CMC/St (90%/10%) blend solutions were prepared by dissolving 0.9 g CMC in 40 mL DD water by stirring for 2.0 h at 85 °C and then dissolved in 0.1 g St/10 mL DD water, and the stirring continued for 1.0 h. Using magnetic stirring and ultrasonication, composite (CMC/St/ $\text{SeO}_2$ ) solutions were prepared by adding the required amount of  $\text{SeO}_2$  NP inside the blend solution. The CMC/St blend and CMC/St/ $\text{SeO}_2$  solutions were cast in cleaned glass Petri dishes and dried slowly at 35–40 °C for several days.

### Characterization and measurements

The PANalytical's X'Pert PRO X-ray diffractometer was operated to record XRD patterns of  $\text{SeO}_2$  powder, CMC/St, and CMC/St/ $\text{SeO}_2$  films. This is done using the  $\text{Cu-K}_\alpha$  radiation of wavelength 1.54 Å, 30 kV, and 30 mA, and in the  $2\theta$  range of 5°–80°. A high-resolution transmission electron microscope (TEM) (JEM 2100/Jeol/Japan) was used to look at the shape and size of the  $\text{SeO}_2$  powder particles. The surface morphology of the films combined with their thickness through the cross-sectional investigation was analyzed using field emission scanning electron microscopy (FE-SEM) coupled with EDAX, supplied by Carl ZEISS Sigma 500 VP. Fourier transform infrared (FTIR)/attenuated total reflection (ATR) analysis was performed in the range 4000–400  $\text{cm}^{-1}$  with a VERTEX 70/70v spectrometer from Bruker Corporation, Germany, and Platinum Diamond ATR. The UV-vis-NIR transmittance and reflectance spectra, in the range of  $\lambda = 200$ –1600 nm, were obtained using a JASCO 630 spectrophotometer. All these measurements were carried out RT. A Keithley 2635A computerized system was used to measure the current–voltage (I–V) characteristics of the CMC/St blend and the CMC/St/ $\text{SeO}_2$  nanocomposite films. The temperature range was 300–415 K, and the voltage range was 0.5–20 V. Two Al electrodes were used on both surfaces of the films to make good contact.

## Results and discussion

### Structural and morphological investigation

XRD patterns of CMC/St, CMC/St/ $\text{SeO}_2$  films, and  $\text{SeO}_2$  powder are presented in Fig. 1. The pure blend and nanocomposite films exhibit a broad peak around  $2\theta = 23.5^\circ$ . This peak confirms the semicrystallinity of the blend. It was reported that the XRD pattern of CMC has a wide and broad peak centered at  $2\theta = 20.7^\circ$ <sup>25</sup>. The observed shift of the main peak of the blend to  $2\theta = 23.5^\circ$  suggests the existence of interactions and intermolecular hydrogen bonding among the chains of CMC and St<sup>8</sup>. Salem et al.<sup>2</sup> also found a broad peak centered at  $2\theta = 22.13^\circ$  in XRD patterns of CMC/polypyrrole. In addition, the observed decrease in the peak intensity, *i.e.*, the peak became broader, after loading 0.1–0.3 wt%  $\text{SeO}_2$  NP indicates the increase of the amorphous regions in the nanocomposite films. The decrease in film crystallinity, as a result of the interactions between CMC/St

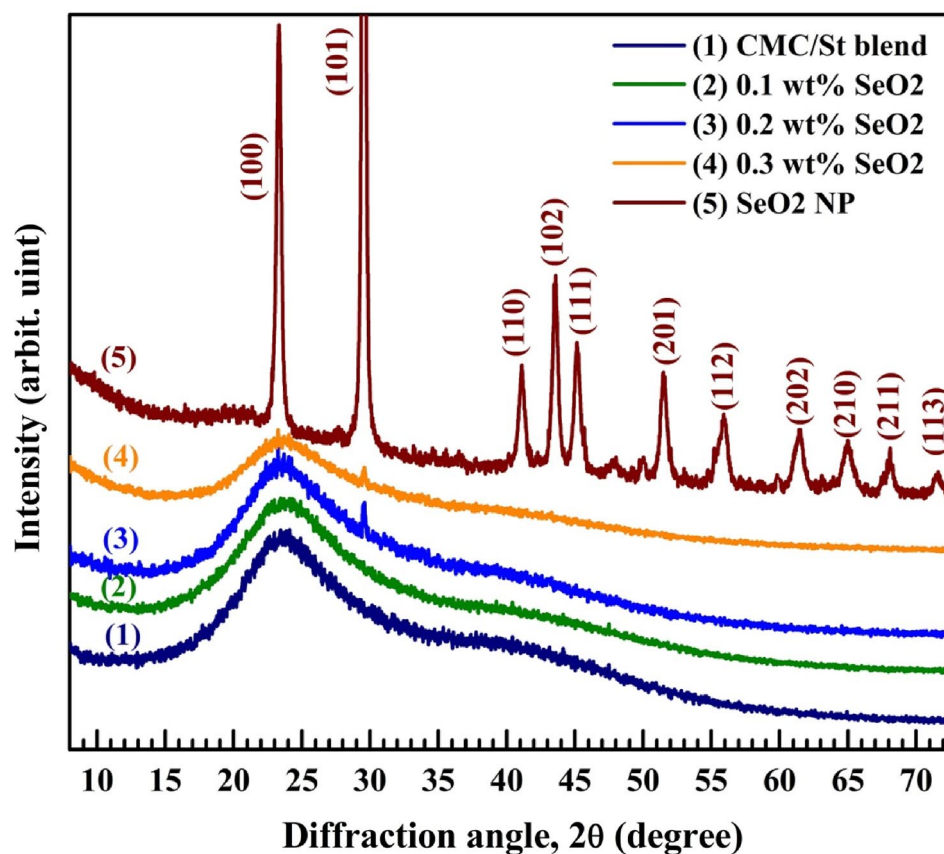


**Figure 1.** XRD patterns of CMC/St, CMC/St/SeO<sub>2</sub> nanocomposites and SeO<sub>2</sub> NP.

chains and the SeO<sub>2</sub>, means more flexibility and improved optical and electrical properties, as will be discussed in the following sections.

The XRD pattern of SeO<sub>2</sub> NP is also shown in Fig. 1. The peaks seen at  $2\theta = 23.38^\circ, 29.39^\circ, 41.19^\circ, 43.51^\circ, 45.49^\circ, 51.51^\circ, 55.79^\circ, 61.39^\circ, 65.05^\circ, 67.96^\circ, 71.41^\circ,$  and  $76.79^\circ$  are assigned to the (100), (101), (110), (102), (111), (201), (112), (202), (210), (211), (113), and (212) diffraction planes, respectively. These peaks or planes match well with those of the crystalline SeO<sub>2</sub>, consistent with JCPDS card no. 06–0362<sup>26</sup>. A similar finding was reported for SeO<sub>2</sub> spherical NP prepared from sodium selenite and some plant leaves<sup>24</sup>. The crystallite size ( $D$ ) of these particles was determined using the well-known Scherrer's equation and found to be 15.9 nm. XRD patterns of the blend loaded with 0.2 and 0.3 wt% SeO<sub>2</sub> contain a small peak at  $29.39^\circ$ , which belongs to the most intense (101) crystalline plane of SeO<sub>2</sub> NP. Other planes disappeared in amorphous regions of the CMC/St blend and were not detected due to the detection limit of the XRD technique. This result confirms the successful incorporation of SeO<sub>2</sub> NP inside CMC/St blend chains.

The morphology of SeO<sub>2</sub> NP was investigated using HR-TEM, as shown in Fig. 2. The SeO<sub>2</sub> nanopowder is composed of NP of spherical shapes having diameters in the range of 10.52–23.44 nm, with an average particle size of 16.88 nm. The inset of Fig. 2 displays the selected area electron diffraction (SAED) of a single particle. The white rings are the result of electron diffraction, which verifies the prepared SeO<sub>2</sub> NP's good crystallinity. These results are consistent with the XRD results. FE-SEM images for the film surface are shown in Fig. 3. The insets of this figure show the cross-sectional view taken for film thickness determination. All films are nonporous, crack-free, and have a thickness ( $d$ ) in the range of 134–150  $\mu\text{m}$ , as listed in Table 1. The CMC/St blend appears homogenous and clear (Fig. 3a). This indicates the CMC and St are mixed and harmonious together, which suggests a good ordering structure. Figure 3b–d shows the uniform distribution of SeO<sub>2</sub> NP on the film surface and dispersion within the blend. Increasing the SeO<sub>2</sub> level to 0.3 wt% SeO<sub>2</sub> results in the formation of small clusters on the film surface. Due to the high surface energy of NP, the SeO<sub>2</sub> particles tend to agglomerate, although they are thickly coated with the CMC/St chains. This result illustrates that the SeO<sub>2</sub> NP are strongly adhered to the CMC/St matrix, which in turn influences the physical properties of the blend. Fig. S1 shows the EDAX spectra of the CMC/St pure blend and that loaded with 0.3 wt% SeO<sub>2</sub> NP. The films are composed of oxygen ( $K_{\alpha 1}$  at 0.27 keV) and carbon ( $K_{\alpha 1}$  at 0.53 keV). The film loaded with 0.3 wt% SeO<sub>2</sub> exhibits two small peaks at 1.37–1.42 keV, representing the  $L_{\alpha}$  and  $L_{\beta}$  lines of Se. In addition, the inset of Fig. S1 confirms the uniform distribution of Se atoms.

This paragraph is devoted to exploring the existing functional groups in the films and discussing their vibrational modes through analyzing the FTIR spectra shown in Fig. 4. The broad absorption band centered around

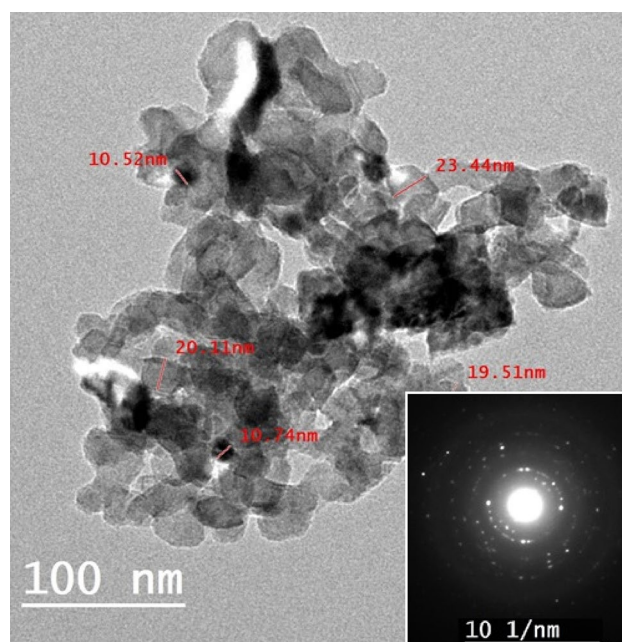


**Figure 2.** HR-TEM image for  $\text{SeO}_2$  NP. The inset is the SAED for a single particle.

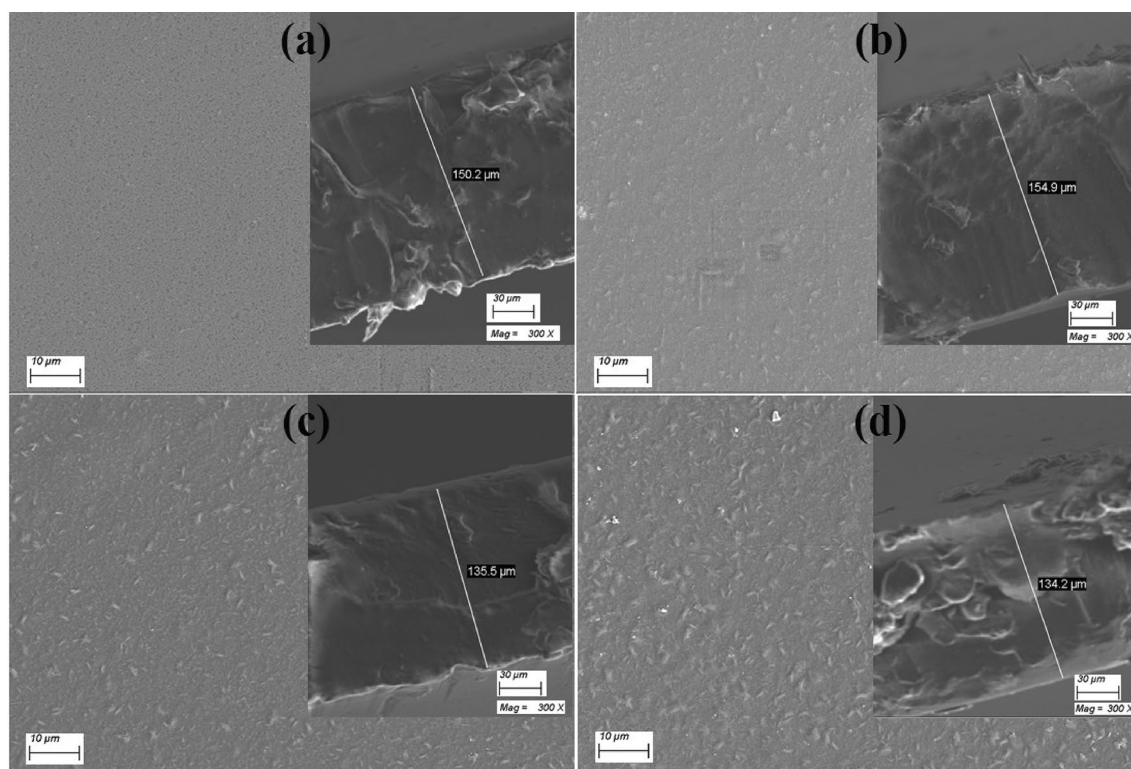


**Figure 3.** FE-SEM surface images for (a) CMC/St, and (b–d) CMC/St loaded with 0.1–0.3 wt%  $\text{SeO}_2$  NP. The insets are the cross-sectional investigation and film thickness evaluation.

$3250\text{ cm}^{-1}$  is assigned to OH stretching, where both CMC and St have many OH groups. The asymmetric stretching vibration of  $\text{CH}_2$  is found at about  $2905\text{ cm}^{-1}$ . The relatively small band at  $1655\text{ cm}^{-1}$  and the sharp one at  $1595\text{ cm}^{-1}$  are assigned to the stretching vibration of the C=O groups of St and CMC ( $\text{COO}^-$  groups)<sup>4</sup>. The  $\text{CH}_2$  scissoring, wagging, and twisting modes in the CMC/St blend take place at  $1410\text{ cm}^{-1}$ ,  $1320\text{ cm}^{-1}$ , and  $1021\text{ cm}^{-1}$ , respectively<sup>27</sup>. The tiny peak in the blend spectrum at  $1095\text{ cm}^{-1}$  may be assigned to the C—C stretching mode<sup>28</sup>. The stretching vibration mode of the  $-\text{CH}_2-\text{OH}$  (primary alcoholic) is observed as a deep and sharp band at

| Sample                   | $E_g$ (eV) |          | $E_o$ (eV) | $E_d$ (eV) | $(N/m^*) \times 10^{26}/\text{kg/m}^3$ |
|--------------------------|------------|----------|------------|------------|--|
|                          | Direct     | Indirect |            |            |  |
| Pure CMC/St              | 5.50       | 4.8      | 5.07       | 10.55      | 0.318                                  |
| 0.1 wt% SeO <sub>2</sub> | 5.40       | 4.6      | 4.23       | 11.44      | 0.972                                  |
| 0.2 wt% SeO <sub>2</sub> | 5.10       | 4.3      | 4.76       | 18.31      | 0.986                                  |
| 0.3 wt% SeO <sub>2</sub> | 5.25       | 4.5      | 5.097      | 25.48      | 1.021                                  |

**Table 1.** Band gap ( $E_g$ ), the average excitation energy ( $E_o$ ), the dispersion energy ( $E_d$ ), and the ratio of carriers' concentration to the electron effective mass ( $N/m^*$ ) of CMC/St/SeO<sub>2</sub>.

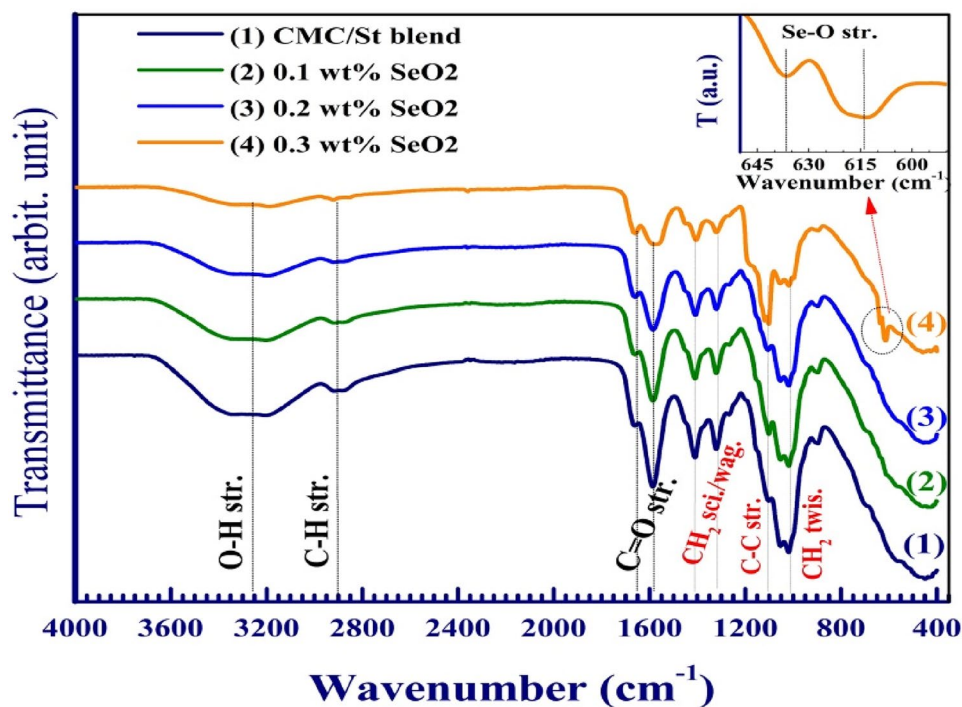


**Figure 4.** Transmission spectra (FTIR) for CMC/St, and CMC/(0.1–0.3 wt%) SeO<sub>2</sub> NP.

1056  $\text{cm}^{-1}$ . Loading 0.1–0.3 wt% SeO<sub>2</sub> NP results in a reduction in the intensity of all bands except the one at 1095  $\text{cm}^{-1}$ , due to the hydrogen bond formed between SeO<sub>2</sub> NP and the functional groups in the blend. The interactions between CMC, St, SeO<sub>2</sub> NP and the hydrogen bonds formed are proposed in Fig. S2. The CMC/St blend has a lot of OH groups, which make it easier for molecules to interact with each other and for hydrogen bonds to form between the blend chains and the added NP. The spectrum of the CMC/St blend loaded with 0.3 wt% SeO<sub>2</sub> has two additional adjacent small bands, as indicated in the inset of this figure, which appear at 636 and 614  $\text{cm}^{-1}$  which could be attributed to Se–O bond vibration<sup>26</sup>. We expect that the changes in structure, hydrogen bonds, and complexation with the added NP will make the blend's physical (electrical and optical) properties better<sup>28</sup>. This will make it useful for a wide range of practical and technological uses.

#### UV–vis spectroscopy and the optical constants

The spectra of transmittance (T%) and reflectance (R%) in the UV–vis–NIR were recorded and used to figure out the changes in the band gap structure and optical constants after adding the SeO<sub>2</sub> NP in the CMC/St blend. Figure 5a displays T% of the films. In visible and IR regions, the blend and 0.3 wt% SeO<sub>2</sub>/blend exhibit 50–90% and 33–74% transmittance, respectively. These ranges of T% make these films suitable for optoelectronic applications. El Miri et al.<sup>14</sup> reported T% between 80 and 95% in the visible light for CMC/St modified with cellulose nanocrystals. The drop in T% as the content of SeO<sub>2</sub> increased is attributed to the sphere-like morphology of SeO<sub>2</sub> NP, seen in Fig. 2. These NP scatter photons that hit them. The T% data were utilized for calculating the absorption coefficient ( $\alpha$ ) using the equation:  $\alpha = \frac{1}{d} \ln \left( \frac{1}{T} \right)$ . Tauc's relations:  $(\alpha hv)^2 = A (hv - E_g^d)$  and  $(\alpha hv)^{1/2} = B (hv - E_g^i)$ , where A and B are constants, and  $hv$  is the incident photon energy,  $hv(\text{eV}) = \frac{1242}{\lambda(\text{nm})}$ , can be used to calculate the direct ( $E_g^d$ ) and indirect ( $E_g^i$ ) band gaps of the samples<sup>16,23</sup>. Figure 5b, c shows the

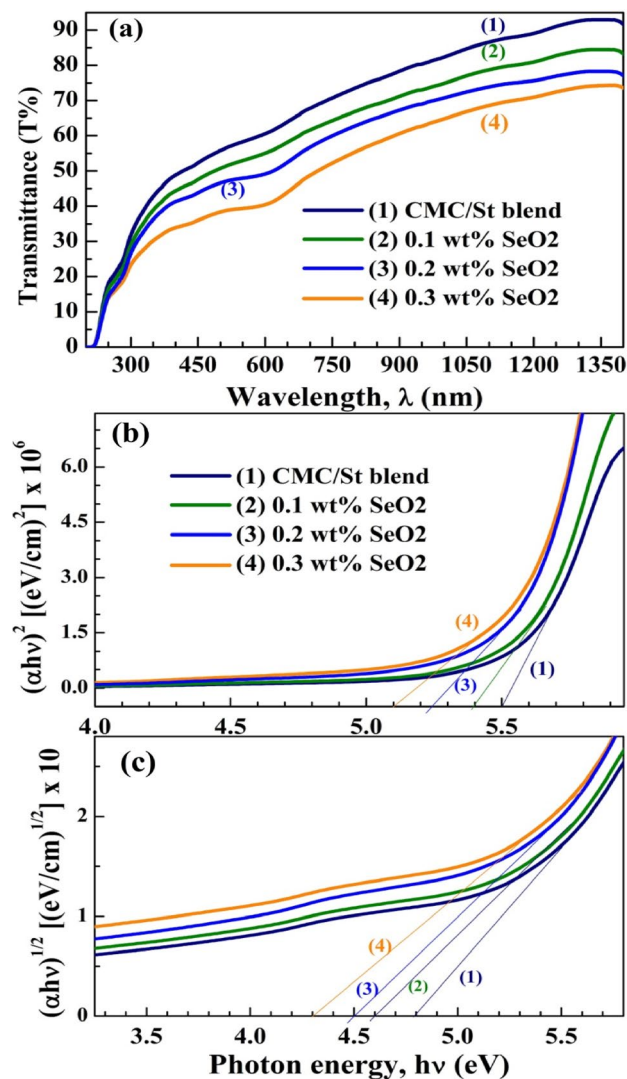


**Figure 5.** UV–vis optical properties; (a) transmittance spectra, (b) direct and (c) indirect band gap.

curves of  $(\alpha hv)^2$  versus  $hv$  and  $(\alpha hv)^{1/2}$  versus  $hv$ . Extrapolating the linear portions of these curves to  $\alpha = 0$ , gives the values of  $E_g^d$  and  $E_g^i$ , which are listed in Table 1. The  $E_g^d$  and  $E_g^i$  of the St/Cs blend are 5.5 and 4.8 eV, respectively, shrank to 5.1 and 4.3 eV, respectively, with increasing the  $\text{SeO}_2$  NP content to 0.3 wt%. Similarly, the  $E_g^d$  and  $E_g^i$  of chitosan (70%)/PAAm (30%) were reduced from 5.32 and 5.03 eV to 5.2 and 4.83 eV, respectively, after loading 2.0 wt% Se NP<sup>23</sup>. In addition, the  $E_g^i$  and  $E_g^d$  of PVA/CMC were decreased from 4.0 and 4.84 eV to 2.18 and 2.96 eV, respectively, after loading 0.8 wt%  $\text{SeO}_2$ <sup>3</sup>. Moreover, the  $E_g^d$  value chitosan/St decreased to 2.23 eV after doping with  $\text{Sb}_2\text{S}_3$ - $\text{CeO}_2$  NP<sup>10</sup>. Hamza and Habeeb reported T% for PVA/CMC blend loaded with 8 wt%  $\text{Cr}_2\text{O}_3$ - $\text{SiO}_2$  NP in the range of 20–50%, and  $E_g^i$  in the range of 4.26–2.91 eV<sup>29</sup>. It's possible for defects to form and for charge transfer complexes and localized states to exist around the blend's valence and conduction bands because of the  $\text{SeO}_2$  NP.

The absorption index ( $k = \frac{\alpha \lambda}{4\pi}$ ) spectra of the blend and nanocomposites are shown in Fig. 6a. The films exhibit very low  $k$  values, where  $k < 3.5 \times 10^{-4}$  in the UV region and  $k < 1 \times 10^{-4}$  in the visible and IR regions. Besides a slight absorption band at 275 nm, a clear absorption edge appears at about 208 nm for all samples; see the inset of this figure. These bands arise due to  $\pi \rightarrow \pi^*$  (C=C/C=O) and  $n \rightarrow \pi^*$  (C-O/C-H) electronic transitions. The noticeable intensity change of these bands between the CMC/St and CMC/St/ $\text{SeO}_2$  may be owing to the increase in disorder and amorphous regions caused by  $\text{SeO}_2$  NP loaded inside the host matrix<sup>30,31</sup>. Moreover, the 0.2 and 0.3 wt%  $\text{SeO}_2$ -loaded films display a hump around 600 nm that could be assigned to the formation of charge transfer complexes. Similar observations were found in the absorption spectrum of PVA/ $\text{Cr}_2\text{O}_3$ <sup>32</sup> and in the spectrum of Cs/PAAm/0.4 wt% Se nanocomposites<sup>24</sup>.

Evaluating the optical constants for the samples, such as the refractive index ( $n$ ), where  $n = \frac{\text{speed of light in the sample}}{3 \times 10^8 \text{ m/s}}$ , is essential for optical communications and device fabrication. The obtained reflectance (R%) spectra were used

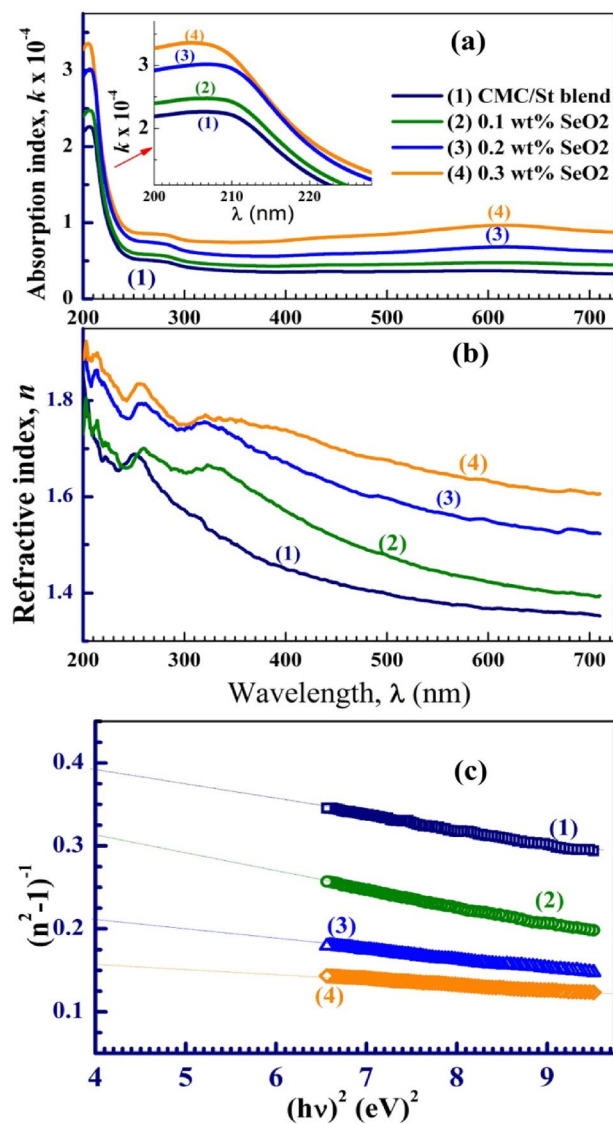


**Figure 6.** Optical constants of CMC/St/SeO<sub>2</sub> nanocomposites; (a) absorption index ( $k$ ), (b) refractive index ( $n$ ), (c) determination of  $E_d$  and  $E_o$ .

to calculate the  $n$  values of the films using the equation:  $n = \frac{1 + \sqrt{R^{33}}}{1 - \sqrt{R}}$ . The distribution of  $n$  with  $\lambda$  is shown in Fig. 6b. In the studied range of  $\lambda$ ,  $2 < n < 1.3$ , where the values of  $n$  take a wave-like behavior in the UV region and decrease with  $\lambda$  in the visible region of the spectrum. The improved reflectivity of the material after the incorporation of SeO<sub>2</sub> NP inside the blend is due to the scattering effect of the dispersed NP. This enhancement in  $n$  values makes CMC/St/SeO<sub>2</sub> composites suitable for some top-end advanced optical and electronic equipment such as anti-reflective coatings, waveguides, and light-emitting diodes.

The average excitation energy ( $E_o$ ) for the electronic transitions, the dispersion energy  $E_d$ , the carriers' concentration divided by the electron effective mass ( $N/m^*$ ), and the optical conductivity ( $\sigma_{op}$ ) are other optical constants important for designing the optoelectronic components and devices. These parameters can be evaluated by looking at how  $n$  decreases with  $\lambda$  (Fig. 7b) and how well they fit the Wemple and Di-Domenico theory. They can also be found using the following relationships<sup>34–36</sup>:

$$(n^2 - 1) = \frac{E_d E_o}{E_o^2 - (h\nu)^2} \quad (1)$$

$$n^2 = \epsilon_l - \lambda^2 \left( \frac{e^2}{\pi c^2} \right) \left( \frac{N}{m^*} \right) \quad (2)$$

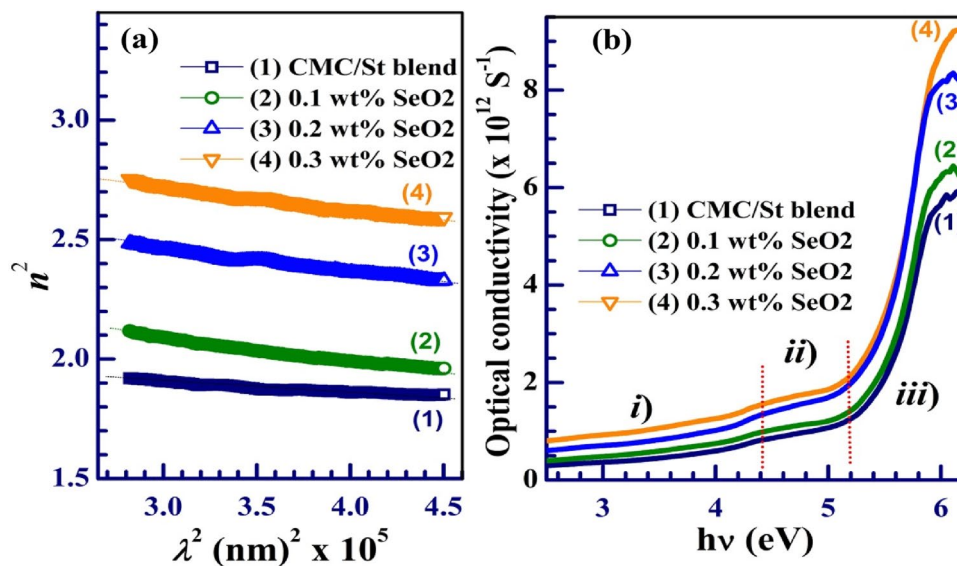


**Figure 7.** (a)  $N/m^*$  determination, and (b) optical conductivity versus the photon energy of CMC/St/SeO<sub>2</sub> nanocomposites.

$$\sigma_{op} = \frac{\alpha nc}{4\pi} \quad (3)$$

where  $\epsilon_L$ ,  $e$ , and  $c$  are the lattice dielectric constant, electron charge, and velocity of light, respectively. The  $E_g$  and  $E_d$  were obtained from the intercepts and slopes of the linear portions of the  $(n^2-1)^{-1}$  versus  $(h\nu)^2$  plots, as shown in Fig. 6c. The  $N/m^*$  values were determined from the slope of Fig. 7a, and the obtained values are listed in Table 1. The gradual increase in  $N/m^*$  values from  $0.318 \times 10^{56}/\text{kg}/\text{m}^3$  for the pure blend to  $1.021 \times 10^{56}/\text{kg}/\text{m}^3$  at 0.3 wt% SeO<sub>2</sub> NP loading is consistent with the observed narrowing in the  $E_g$ . This means improving the semiconducting nature of the CMC/St blend with SeO<sub>2</sub> NP incorporation. Figure 7b shows the dependence of  $\sigma_{op}$  on  $h\nu$ . To explain the observed behavior of  $\sigma_{op}$ , the curves can be divided into three regions. (i) The  $\sigma_{op}$  increases slightly with  $h\nu$  till  $h\nu < 4.4$  eV, where these limited energy values can excite a small number of the charge carriers to participate in the conduction process. (ii) A plateau region ( $4.4 < h\nu < 5.2$  eV),  $\sigma_{op}$  values appear constant. In region (iii) the incident energy ( $h\nu > 5.2$  eV) is larger than the direct  $E_g$ , so that  $\sigma_{op}$  increases sharply, where the photons of the UV region have enough energy to excite the charge carriers to higher energy levels<sup>37</sup>. In this region,  $\sigma_{op}$  of the films is in the range of  $2 \times 10^{12}$ – $6 \times 10^{12} \text{ S}^{-1}$ , which is larger than the values of  $0.95 \times 10^{12}$ – $1.68 \times 10^{12} \text{ S}^{-1}$  reported for PVA/CMC blend loaded with Cr<sub>2</sub>O<sub>3</sub>–SiO<sub>2</sub> NP up to 8.0 wt%<sup>29</sup>. Moreover,  $\sigma_{op}$  of CMC was found to be less than  $2.0 \times 10^{11} \text{ S}^{-1}$  increased to be in the range of  $4.0 \times 10^{12} \text{ S}^{-1}$ – $6.0 \times 10^{12} \text{ S}^{-1}$  after blending with polypyrrole<sup>2</sup>. This means that St greatly improves the  $\sigma_{op}$  of CMC. At  $h\nu > 6.0$  eV a saturation state is reached. SeO<sub>2</sub> NP loading induced structural changes, defect states, and charge transfer complex formation, as discussed in the previous sections. Therefore, a significant improvement in  $\sigma_{op}$  with increasing SeO<sub>2</sub> NP content is noticed. The changes that SeO<sub>2</sub> NP caused in the optical parameters show that they are effective for improving the optical properties of the CMC/St blend. These enhancements make these compositions suitable for optoelectronic devices like photovoltaic cells and organic light-emitting diodes<sup>38</sup>.

### ***I–V Characteristics, conductivity, and conduction mechanism***

The  $I$ – $V$  characteristic curves of the CMC/St blend and its nanocomposites are shown in Fig. 8a–d. In the applied volts range of 0.5–20 V, the obtained  $I$  is increased with increasing the temperatures to a certain degree: 390 K for blend, 0.1 and 0.3 wt% SeO<sub>2</sub> NP-loaded films, and 400 K at 0.2 wt% SeO<sub>2</sub> content. After this limit,  $I$  decreased with increasing temperature. This behavior indicates that the temperature has a decisive effect on  $I$ , whatever the applied voltage. All films permit a current in the order of  $10^{-5}$  A, but the SeO<sub>2</sub> NP-loaded films have a higher  $I$ . The relation:  $I = FV^r$ <sup>39</sup>, where  $F$  is a constant, can be used to determine the nonlinear coefficient parameter ( $r$ ) for reporting the conduction mechanism in polymers<sup>40</sup>. When  $r = 1$ , then the ohmic behavior is dominant. A value of  $r = 2$  means that trap-free-space-charge-limited is the leading mechanism. For  $r > 2$ , the space-charge-limited mechanism could be a suitable conduction mechanism<sup>41</sup>. The  $r$  values are derived from the slope on the linear portions of  $\text{Ln}(I)$ – $\text{Ln}(V)$  curves, as depicted in Fig. S3 and listed in Table S1. As noticed,  $r$  values are in the range of 1.06–1.95, 1.45–1.95, 1.63–2.14, and 2.07–2.23 for the blend pure and loaded with 0.1, 0.2, and 0.3 wt% SeO<sub>2</sub> NP, respectively. These values confirm the non-ohmic feature of the  $I$ – $V$  characteristics of the materials under study. Increasing  $r$  after doping implies that the traps become larger or deeper.

Figure 9a–d shows the dependence of dc conductivity ( $\sigma_{dc}$ ) on the temperatures as  $\text{Ln}(\sigma_{dc})$  versus  $(1000/T)$ , verifying the Arrhenius relation<sup>42</sup>:

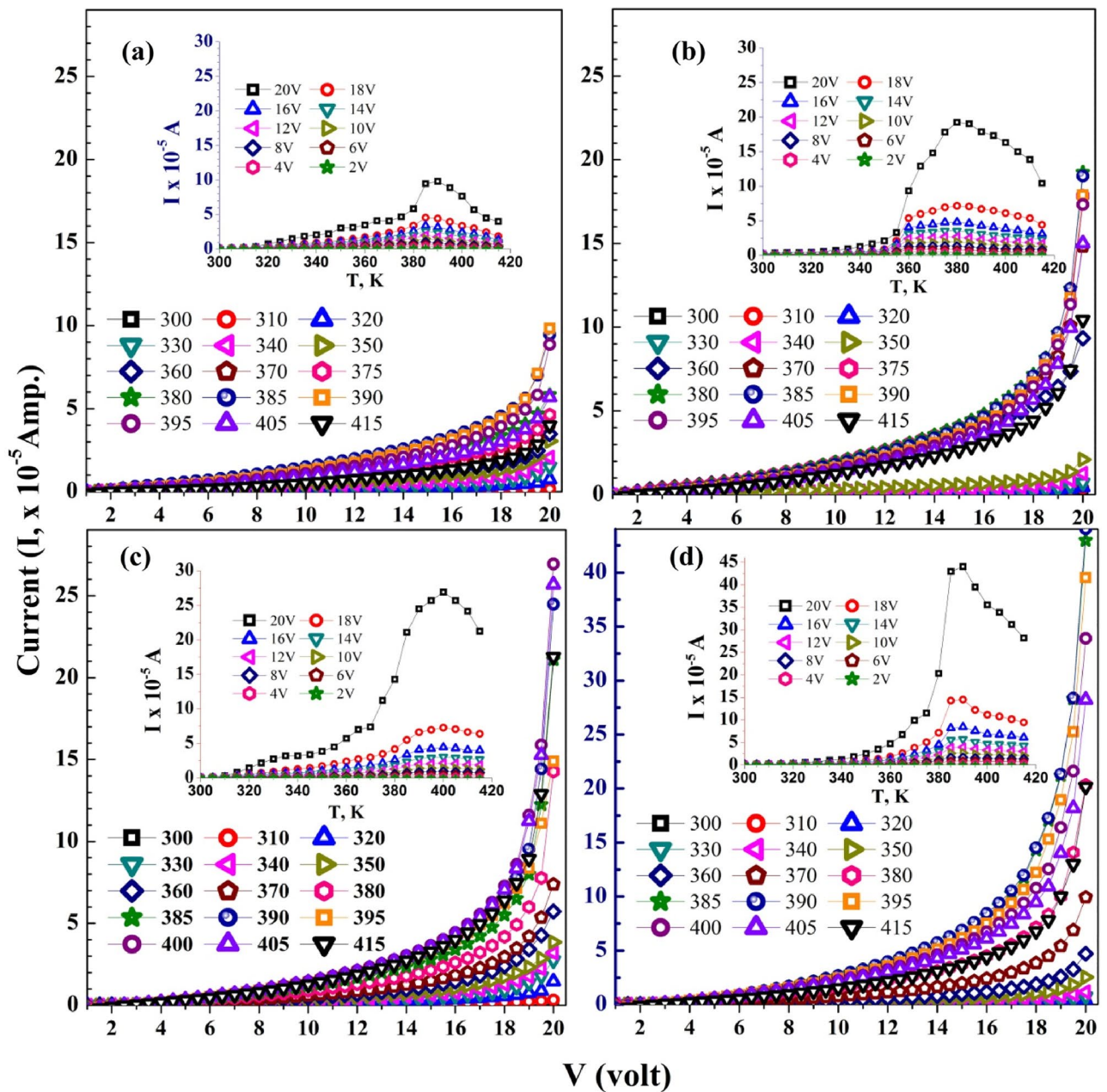


**Figure 8.** I–V curves in the temperature range of 300–415 K for (a) the blend, and (b–d) the blend loaded with 0.1–0.3 wt% SeO<sub>2</sub> NP. The insets show the variation of *I* with *T* at 2.0–20 V.

$$\sigma_{dc} = \sigma_0 \exp\left(\frac{E_a}{k_B T}\right), \quad (4)$$

where  $\sigma_0$  is the conductivity at infinite temperature,  $k_B$  is the Boltzmann constant, and  $E_a$  is the activation energy. The  $\sigma_{DC}$  of the investigated films was calculated by using the relation;  $\sigma_{dc} = \frac{I \cdot d}{V \cdot A}$ , where  $d$  and  $A$  are the sample thickness and cross-sectional area, respectively. Some notes can be drawn from this figure: (i) The  $\sigma_{dc}$  of the blend varies between  $3.8 \times 10^{-7}$  to  $5.6 \times 10^{-4}$  S/m, according to the applied temperature. These values are consistent with the published results<sup>39</sup>. (ii) The overall temperature dependence of the  $\sigma_{dc}$  curves can be divided into three distinct regions: At low (300–320 K) and moderate (320–380 K) temperatures, the Arrhenius behavior is verified with a high rate of  $\sigma_{dc}$  improvement at low temperatures due to the available thermal activation of the blend chains in this region, followed by a relatively lower rate of  $\sigma_{dc}$  improvement in the moderate region of temperatures. In the third region or high temperatures (380–415 K), a decrement trend in  $\sigma_{dc}$  is observed. The blend loaded with 0.2 wt% SeO<sub>2</sub> NP exhibits similar behavior to that of the blend but with higher and constant  $\sigma_{dc}$  at higher temperatures (385–415 K). The  $\sigma_{dc}$  curves of the 0.1 and 0.3 wt% SeO<sub>2</sub> NP blend are divided into two regions only; the first one extends in the regions of 300–360 K and 300–380 K, where  $\sigma_{dc}$  increases with temperature. The second one is at temperatures in the range of 360–415 K for 0.1 wt% SeO<sub>2</sub> and 380–415 K for 0.3 wt% SeO<sub>2</sub>.

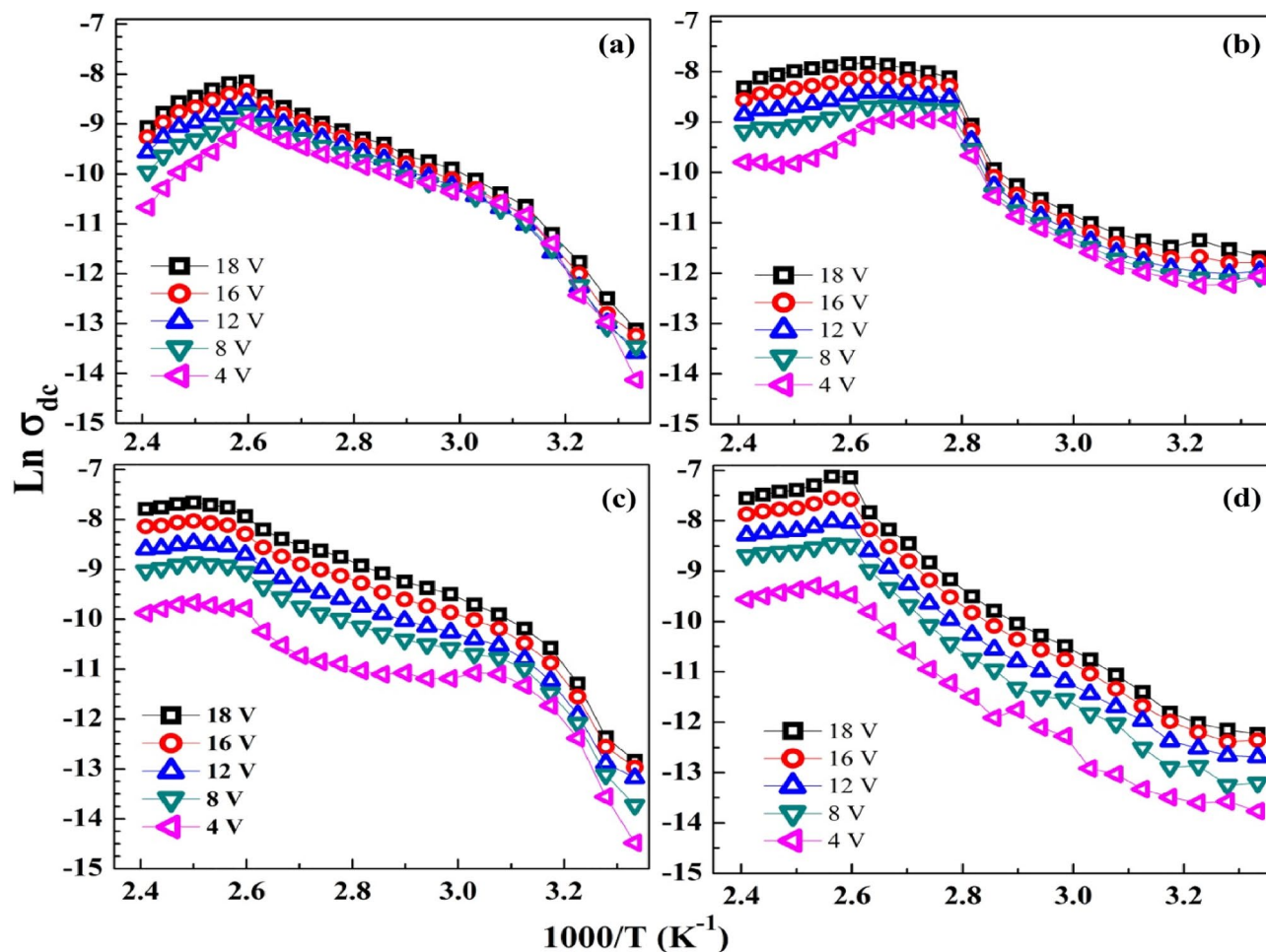


**Figure 9.** Variation of  $\text{Ln}(\sigma_{dc})$  with  $(1000/T)$  for (a) CMC/St blend and (b–d) blend loaded with 0.1–0.3 wt%  $\text{SeO}_2$  NP.

content, where  $\sigma_{DC}$  decreases at a low rate with temperature. At the higher side of temperatures,  $\sigma_{DC}$  of 0.3 wt%  $\text{SeO}_2/\text{blend}$   $\sigma_{dc}$  of 0.1 wt%  $\text{SeO}_2$  blend  $\sigma_{dc}$  of the blend. This means increasing  $\text{SeO}_2$  NP content results in raising  $\sigma_{dc}$  of the blend. This result is consistent with the XRD and UV/vis data, where the reduced crystallinity and increasing disorder made the  $E_g$  of the blend more shrinkable with an increasing  $\text{SeO}_2$  NP ratio. The uniform distribution of  $\text{SeO}_2$  NP facilitates the formation of a continuous network throughout the blend matrix.

To shed more light on the conduction mechanism, we will consider the following relations between the current density ( $J = \frac{I}{A}$ ) and the applied electric field ( $E = \frac{V}{d}$ )<sup>43,44</sup>: for the Schottky (Sc) mechanism:

$$J = GT^2 \exp\left(-\frac{\varphi}{k_B T}\right) \exp\left(\frac{\beta(\text{Sc})E^{0.5}}{k_B T}\right), \quad (5)$$

and Poole–Frenkel (PF) mechanism:

$$J = \frac{\sigma_o V}{d} \exp\left(\frac{\beta(\text{PF})E^{0.5}}{k_B T}\right) \quad (6)$$

where  $T$  is the absolute temperature,  $k_B = 1.379 \times 10^{-23}$  J/K (Boltzmann constant),  $G$ , and  $\varphi$  are constants, and  $\sigma_o$  is the low field conductivity. The Sc emission is related to the barrier at the surface of a metal or insulator, whereas the PF emission is related to the barrier in the bulk of the material. Theoretically, it was concluded that:

$$\beta(\text{Sc}) = \sqrt{\frac{e}{4\pi \epsilon_o \epsilon'}} \quad \text{and} \quad \beta(\text{PF}) = \sqrt{\frac{e}{\pi \epsilon_o \epsilon'}}, \quad (7)$$

where  $\epsilon_o$  is the permittivity of free space and  $\epsilon'$  is the permittivity of the material. This means that  $\beta(\text{PF}) = 2\beta(\text{Sc})$ . For our blend, we can take  $\epsilon' = 5^{45}$ , the  $\beta(\text{Sc})$  and  $\beta(\text{PF})$  should be in the order of  $1.69 \times 10^{-5}$  and  $3.39 \times 10^{-5}$ , respectively.

Fig. S4 and Fig. 10a–d display the curves of  $\text{Ln}(J)$  versus  $E^{0.5}$  and  $\text{Ln}(J/E)$  versus  $E^{0.5}$ , respectively, for the blend and its nanocomposites. The  $\beta(\text{Sc})$  and  $\beta(\text{PF})$  values were determined on the slopes of Fig. S4 and Fig. 10a–d,

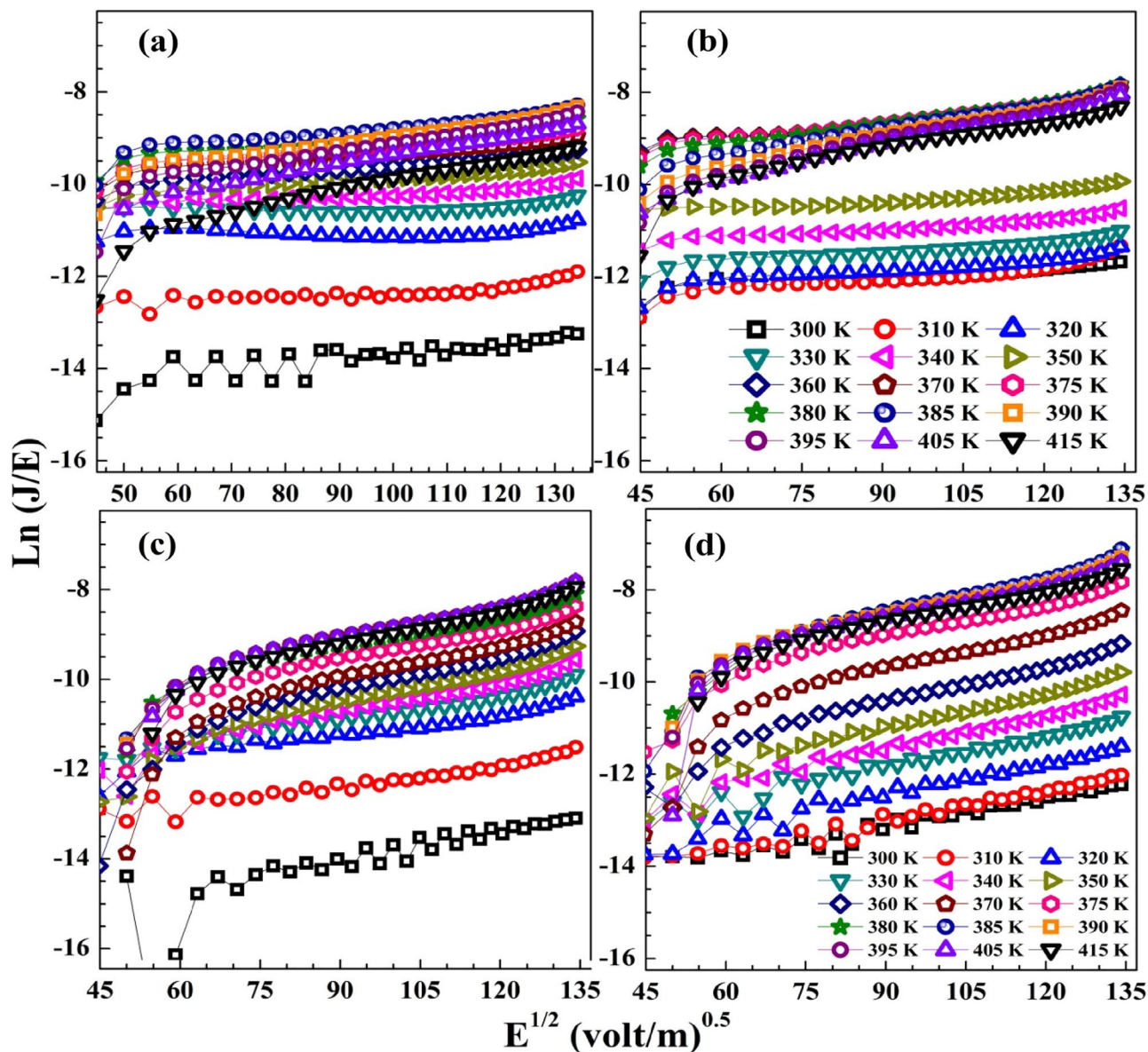


**Figure 10.**  $\ln(J/E)$  versus  $E^{0.5}$  to determine the conduction mechanism in (a) CMC/St blend and (b–d) the blend loaded with 0.1–0.3 wt%  $\text{SeO}_2$  NP.

| Sample                    | $\beta$ value      | at                    |                       |                       |                       |
|---------------------------|--------------------|-----------------------|-----------------------|-----------------------|-----------------------|
|                           |                    | 300 K                 | 310 K                 | 330 K                 | 350 K                 |
| CMC/St blend              | $\beta(\text{PF})$ | $3.68 \times 10^{-5}$ | $8.14 \times 10^{-5}$ | $1.89 \times 10^{-5}$ | $6.60 \times 10^{-5}$ |
|                           | $\beta(\text{Sc})$ | $1.64 \times 10^{-4}$ | $1.27 \times 10^{-4}$ | $1.31 \times 10^{-4}$ | $1.68 \times 10^{-4}$ |
| 0.1 wt% $\text{SeO}_2$ NP | $\beta(\text{PF})$ | $4.14 \times 10^{-5}$ | $3.62 \times 10^{-5}$ | $3.72 \times 10^{-5}$ | $2.50 \times 10^{-5}$ |
|                           | $\beta(\text{Sc})$ | $1.69 \times 10^{-4}$ | $1.5 \times 10^{-4}$  | $1.5 \times 10^{-4}$  | $1.34 \times 10^{-4}$ |
| 0.2 wt% $\text{SeO}_2$ NP | $\beta(\text{PF})$ | $1.37 \times 10^{-5}$ | $8.98 \times 10^{-5}$ | $7.48 \times 10^{-5}$ | $5.10 \times 10^{-5}$ |
|                           | $\beta(\text{Sc})$ | $2.26 \times 10^{-4}$ | $1.91 \times 10^{-4}$ | $1.82 \times 10^{-4}$ | $2.20 \times 10^{-4}$ |
| 0.3 wt% $\text{SeO}_2$ NP | $\beta(\text{PF})$ | $5.41 \times 10^{-5}$ | $6.23 \times 10^{-5}$ | $6.23 \times 10^{-5}$ | $5.17 \times 10^{-5}$ |
|                           | $\beta(\text{Sc})$ | $2.68 \times 10^{-4}$ | $2.44 \times 10^{-4}$ | $2.36 \times 10^{-4}$ | $2.26 \times 10^{-4}$ |

**Table 2.**  $\beta(\text{PF})$  and  $\beta(\text{Sc})$  values derived from the slopes of Fig. 10 and Fig. S4.

respectively, as  $\beta = \text{slope} \times k_B T$ , and the values are listed in Table 2. As noticed, the values of  $\beta$  are consistent with the theoretical value of  $\beta(\text{PF})$ , thus the PF emission is the most suitable conduction mechanism in CMC/St blend, and their composites with 0.1–0.3 wt% SeO<sub>2</sub> NP. The conduction mechanism in the CMC/PVP (75%/25%) blend and NiO/CMC/PVP nanocomposites was found to be PF emission<sup>4</sup>, while in the CMC/PVA (80%/20%) blend it was found to be Sc emission. However, doping with CuO NP into this blend matrix and heating led to the PF emission<sup>25</sup>. Therefore, the mechanism of conduction in polymeric and nanocomposite materials depends on the blend structure, temperature, and nanofillers.

## Conclusion

Well-crystallized SeO<sub>2</sub> NP was solvothermally prepared and loaded within the CMC/St bio-blend. Increasing the SeO<sub>2</sub> level from 0.1 to 0.3 wt% increased the amorphous regions inside the blend. SeO<sub>2</sub> NP with a spherical shape and a crystallite size of 16.88 nm was spread out evenly on the surface of the film and worked well with the functional groups of the blend. At 0.3 wt% SeO<sub>2</sub>, the transmission of the blend decreased from 50–90% to 33–74%, and the direct and indirect band gaps decreased from 5.5 and 4.8 eV to 5.25 and 4.5 eV, respectively. The dispersion optical parameters  $E_o$ ,  $E_d$ ,  $N/m^*$ , and optical conductivity were improved with increasing SeO<sub>2</sub> NP content. All samples exhibited non-ohmic features based on the  $I$ - $V$  characteristics. The  $\sigma_{dc}$  displayed Arrhenius behavior. Increasing the amorphous regions and defects inside the blend and shrinking the band gap and the continuous network formed by SeO<sub>2</sub> NP throughout the blend matrix led to the observed increase in  $\sigma_{dc}$ . Based on the dependence of  $J$  on  $E$  in the temperature range 300–415 K ( $\ln(J/E)$  vs.  $E^{0.5}$ ), Poole–Frenkel emission is found to be the most favorable conduction mechanism in the nanocomposite films. In summary, SeO<sub>2</sub> NP led to structural changes inside the CMC/St blend and improved the optical and electrical properties of the blend. Therefore, the obtained materials are best suited for coatings, optoelectronic applications, and related devices such as photovoltaic cells and organic light-emitting diodes.

## Data availability

The datasets used and/or analyzed during the current study available from the corresponding authors on reasonable request.

Received: 15 September 2023; Accepted: 30 January 2024

Published online: 10 February 2024

## References

- Gaabout, L. H. Effect of selenium oxide nanofiller on the structural, thermal and dielectric properties of CMC/PVP nanocomposites. *J. Mater. Res. Technol.* **9**(3), 4319–4325. <https://doi.org/10.1016/j.jmrt.2020.02.057> (2020).
- Salem, A. M. *et al.* Effect of polypyrrole on structural, optical and thermal properties of CMC-based blends for optoelectronic applications. *Opt. Mater.* **134**, 113128. <https://doi.org/10.1016/j.optmat.2022.113128> (2022).
- Wang, Y. *et al.* MgO/carboxymethyl chitosan nanocomposite improves thermal stability, waterproof and antibacterial performance for food packaging. *Carbohydr. Polym.* **236**, 116078. <https://doi.org/10.1016/j.carbpol.2020.116078> (2020).
- El Sayed, A. M. & Saber, S. Structural, optical analysis, and Poole–Frenkel emission in NiO/CMC–PVP: Bio-nanocomposites for optoelectronic applications. *J. Phys. Chem. Solids* **163**, 110590. <https://doi.org/10.1016/j.jpcs.2022.110590> (2022).
- Ramesan, M. T. *et al.* Influence of magnetite nanoparticles on electrical, magnetic and thermal properties of chitin/cashew gum biopolymer nanocomposites. *Polym. Compos.* **39**, E540–E549. <https://doi.org/10.1002/pc.24688> (2018).
- Meera, K., Arun, K. & Ramesan, M. T. Nanochitosan reinforced polyvinyl alcohol/cashew gum bio-blend nanocomposites: Promising materials for future frontiers. *J. Polym. Environ.* **31**, 4487–4505. <https://doi.org/10.1007/s10924-023-02909-8> (2023).
- Meera, K. & Ramesan, M. T. Tailoring the performance of boehmite nanoparticles reinforced carboxymethyl chitosan/cashew gum blend nanocomposites via green synthesis. *Polymer* **268**, 125706. <https://doi.org/10.1016/j.polymer.2023.125706> (2023).
- Morsi, M. A. *et al.* Structural, optical, mechanical, and dielectric properties studies of carboxymethyl cellulose/polyacrylamide/lithium titanate nanocomposites films as an application in energy storage devices. *Polym. Test.* **114**, 107705. <https://doi.org/10.1016/j.polymertesting.2022.107705> (2022).
- Abou Elfadl, A. *et al.* Influence of  $\alpha$ -Fe<sub>2</sub>O<sub>3</sub>, CuO, and GO 2D nano-fillers on the structure, physical properties and antifungal activity of Na-CMC–PAAm blend. *Sci. Rep.* **13**, 12358. <https://doi.org/10.1038/s41598-023-39056-y> (2023).
- Hammami, I. *et al.* Electrical, morphology and structural properties of biodegradable nanocomposite polyvinyl-acetate/cellulose nanocrystals. *Mater. Chem. Phys.* **240**, 122182. <https://doi.org/10.1016/j.matchemphys.2019.122182> (2020).
- Hamza, R. S. A. & Habeeb, M. A. Reinforcement of morphological, structural, optical, and antibacterial characteristics of PVA/CMC bio blend filled with SiO<sub>2</sub>/Cr<sub>2</sub>O<sub>3</sub> hybrid nanoparticles for optical nanodevices and food packing industries. *Polym. Bull.* <https://doi.org/10.1007/s00289-023-04913-3> (2023).
- Wu, W.-C., Hsiao, P.-Y. & Huang, Y.-C. Effects of amylose content on starch–chitosan composite film and its application as a wound dressing. *J. Polym. Res.* **26**, 137. <https://doi.org/10.1007/s10965-019-1770-0> (2019).
- Fekete, T. *et al.* Synthesis of carboxymethylcellulose/starch superabsorbent hydrogels by gamma-irradiation. *Chem. Centr. J.* **11**, 46. <https://doi.org/10.1186/s13065-017-0273-5> (2017).
- El Miri, N. *et al.* Bio-nanocomposite films reinforced with cellulose nanocrystals: Rheology of film-forming solutions, transparency, water vapor barrier and tensile properties of films. *Carbohydr. Polym.* **129**, 156–167. <https://doi.org/10.1016/j.carbpol.2015.04.051> (2015).
- Sun, Z. *et al.* The improved properties of carboxymethyl bacterial cellulose films with thickening and plasticizing. *Polymers* **14**, 3286. <https://doi.org/10.3390/polym14163286> (2022).
- Alghunaim, N. S. Characterization of selenium oxide nanofiller effect on the spectroscopic and thermal properties of Cs/PAM nanocomposites. *J. Mater. Res. Technol.* **9**(3), 3502–3510. <https://doi.org/10.1016/j.jmrt.2020.01.087> (2020).
- Swathi, S. *et al.* Designing rational and cheapest SeO<sub>2</sub> electrocatalyst for long stable water splitting process. *J. Phys. Chem. Solids* **145**, 109544. <https://doi.org/10.1016/j.jpcs.2020.109544> (2020).
- Farooq, F., Din, M. I. & Hussain, Z. Morphologically controlled synthesis of 1-dimensional selenium dioxide and study of its application as catalyst for diesel fuel additive. *Arab. J. Chem.* **15**, 103805. <https://doi.org/10.1016/j.arabjc.2022.103805> (2022).
- Bisht, N., Phalswal, P. & Khanna, P. K. Selenium nanoparticles: A review on synthesis and biomedical applications. *Mater. Adv.* **3**, 1415–1431. <https://doi.org/10.1039/d1ma00639h> (2022).

20. Shakibaie, M. *et al.* Anti-biofilm activity of biogenic selenium nanoparticles and selenium dioxide against clinical isolates of *Staphylococcus aureus*, *Pseudomonas aeruginosa*, and *Proteus mirabilis*. *J. Trace Elem. Med. Biol.* **29**, 235–241. <https://doi.org/10.1016/j.jtemb.2014.07.020> (2015).
21. Fouda, A. *et al.* Light enhanced the antimicrobial, anticancer, and catalytic activities of selenium nanoparticles fabricated by endophytic fungal strain, *Penicillium crustosum* EP-1. *Sci. Rep.* **12**, 11834. <https://doi.org/10.1038/s41598-022-15903-2> (2022).
22. Kazemi, M. *et al.* Evaluation of antifungal and photocatalytic activities of gelatin-stabilized selenium oxide nanoparticles. *J. Inorg. Organomet. Polym. Mater.* **30**, 3036–3044. <https://doi.org/10.1007/s10904-020-01462-4> (2020).
23. Ragab, H. M. *et al.* An insight into the influence of Ag/Se nanoparticles on the structural, optical, and electrical properties of Cs/PAM nanocomposites films as application in electrochemical devices. *J. Molec. Struct.* **1267**, 133619. <https://doi.org/10.1016/j.molstruc.2022.133619> (2022).
24. Gami, F. *et al.* Structural, optical and electrical studies of chitosan/polyacrylamide blend filled with synthesized selenium nanoparticles. *J. Molec. Struct.* **1257**, 132631. <https://doi.org/10.1016/j.molstruc.2022.132631> (2022).
25. El Sayed, A. M. *et al.* Effect of PVA and copper oxide nanoparticles on the structural, optical, and electrical properties of carboxy-methyl cellulose films. *J. Mater. Sci.* **50**, 4717–4728. <https://doi.org/10.1007/s10853-015-9023-z> (2015).
26. Nassar, A. A. *et al.* Exploring the antimicrobial, antioxidant, anticancer, biocompatibility, and larvicidal activities of selenium nanoparticles fabricated by endophytic fungal strain *Penicillium verhagenii*. *Sci. Rep.* **13**, 9054. <https://doi.org/10.1038/s41598-023-35360-9> (2023).
27. Elashmawi, I. S. & Al-Muntaser, A. A. Influence of Co<sub>3</sub>O<sub>4</sub> nanoparticles on the optical, and electrical properties of CMC/PAM polymer: Combined FTIR/DFT study. *J. Inorg. Organ. Polym. Mater.* **31**, 2682–2690. <https://doi.org/10.1007/s10904-021-01956-9> (2021).
28. Awad, S. *et al.* Characterization, optical, and nanoscale free volume properties of Na-CMC/PAM/CNT nanocomposites. *Polym. Adv. Technol.* **31**(1), 114–125. <https://doi.org/10.1002/pat.4753> (2020).
29. Abdul Hamza, R. S. & Habeeb, M. A. Reinforcement of morphological, structural, optical, and antibacterial characteristics of PVA/CMC bioblend filled with SiO<sub>2</sub>/Cr<sub>2</sub>O<sub>3</sub> hybrid nanoparticles for optical nanodevices and food packing industries. *Polym. Bull.* <https://doi.org/10.1007/s00289-023-04913-3> (2023).
30. Saion, E. *et al.* Changes in the optical band gap and absorption edge of gamma-irradiated polymer blends. *J. Appl. Sci.* **5**(10), 1825–1829. <https://doi.org/10.3923/jas.2005.1825.1829> (2005).
31. Elashmawi, I. S., Abdelrazek, E. M. & Yassin, A. Y. Influence of NiCl<sub>2</sub>/CdCl<sub>2</sub> as mixed filler on structural, thermal and electrical properties of PVA/PVP blend. *Br. J. Appl. Sci. Technol.* **4**(30), 4263–4279. <https://doi.org/10.9734/BJAST/2014/12317> (2014).
32. Hassen, A. *et al.* Influence of Cr<sub>2</sub>O<sub>3</sub> nanoparticles on the physical properties of polyvinyl alcohol. *Am. J. Appl. Phys.* **112**, 093525. <https://doi.org/10.1063/1.4764864> (2012).
33. Alanazi, T. I. & El Sayed, A. M. Characterization of Mg–Pb–O systems, and MgPbO–thermoplastic blend: Nanocomposites for photonic and microelectronic devices. *J. Phys. Chem. Solids* **178**, 111346. <https://doi.org/10.1016/j.jpcs.2023.111346> (2023).
34. Khmissi, H., El Sayed, A. M. & Shaban, M. Structural, morphological, optical properties and wettability of spin-coated copper oxide; influences of film thickness, Ni, and (La, Ni) co-doping. *J. Mater. Sci.* **51**, 5924. <https://doi.org/10.1007/s10853-016-9894-7> (2016).
35. El Sayed, A. M. & Mohamad, A. D. M. Synthesis, structural, thermal, optical and dielectric properties of chitosan biopolymer; influence of PVP and  $\alpha$ -Fe<sub>2</sub>O<sub>3</sub> Nanorods. *J. Polym. Res.* **25**, 175. <https://doi.org/10.1007/s10965-018-1571-x> (2018).
36. El Sayed, A. M. Opto-structural and surface properties of silkworm-like nickel oxide thin films. *Mater. Res. Express* **6**, 116423. <https://doi.org/10.1088/2053-1591/ab4663> (2019).
37. El Fewaty, N. H., El Sayed, A. M. & Hafez, R. S. Synthesis, structural and optical properties of tin oxide nanoparticles and its CMC/PEG–PVA nanocomposite films. *Polym. Sci. A* **58**(6), 1004–1016. <https://doi.org/10.1134/S0965545X16060055> (2016).
38. Nguyen, T.-P. Polymer-based nanocomposites for organic optoelectronic devices: A review. *Surf. Coat. Technol.* **206**, 742–752. <https://doi.org/10.1016/j.surfcoat.2011.07.010> (2011).
39. El-Gamal, S. & El Sayed, A. M. Influence of MWCNTs in improving the optical, DC conductivity, and mechanical properties of CMC/PAAM blends. *Polym. Eng. Sci.* **60**(5), 996–1005. <https://doi.org/10.1002/pen.25355> (2020).
40. Abkowitz, M., Facci, J. S. & Rehm, J. Direct evaluation of contact injection efficiency into small molecule based transport layers: Influence of extrinsic factors. *J. Appl. Phys.* **83**, 2670. <https://doi.org/10.1063/1.367030> (1998).
41. Bunakov, A., Lachinov, A. & Salikhov, R. Current-voltage characteristics of thin poly(biphenyl-4-ylphthalide) films. *Macromol. Symp.* **212**, 387. <https://doi.org/10.1002/masy.200450847> (2004).
42. El-Sayed, S. & El Sayed, A. M. Influence of the sol–gel-derived nano-sized TiO<sub>2</sub> and Y<sub>2</sub>O<sub>3</sub> in improving the optical and electric properties of P(VAc/MMA). *Braz. J. Phys.* **51**, 1584–1596. <https://doi.org/10.1007/s13538-021-00979-4> (2021).
43. Hanafy, T. A. Dielectric relaxation and Schottky conduction of IR laser irradiated Makrofol-DE polycarbonate. *J. Appl. Polym. Sci.* **124**, 1–8. <https://doi.org/10.1002/app.34537> (2012).
44. Kumar, A., Das, M., Mukherjee, S. Oxide based memristors: fabrication, mechanism, and application, *Chap. 4, Conduc. Mech. Mem.*, 4–11 (2018). <https://doi.org/10.1016/B978-0-12-803581-8.10384-4>
45. El-Sayed, S. *et al.* DSC, TGA and dielectric properties of carboxymethyl cellulose/polyvinyl alcohol blends. *Physica B* **406**, 4068–4076. <https://doi.org/10.1016/j.physb.2011.07.050> (2011).

## Acknowledgements

The authors extend their appreciation to the Deanship of Scientific Research at Northern Border University, Arar, KSA for funding this research work through the project number “NBU-FFR-2023-0168”. The authors are grateful to the Prince Faisal bin Khalid bin Sultan Research Chair in Renewable Energy Studies and Applications (PFCRE) at Northern Border University for their support and assistance.

## Author contributions

A.M.E.S: the conceptualization, methodology, validation, formal analysis, investigation, resources, data curation, writing-original draft preparation, writing-review and editing, visualization, and publishing the manuscript. T.I.A.: validation, investigation, writing-review, and editing, and publishing the manuscript.

## Competing interests

The authors declare no competing interests.

## Additional information

**Supplementary Information** The online version contains supplementary material available at <https://doi.org/10.1038/s41598-024-53268-w>.

**Correspondence** and requests for materials should be addressed to A.M.E.S. or T.I.A.

**Reprints and permissions information** is available at [www.nature.com/reprints](http://www.nature.com/reprints).

**Publisher's note** Springer Nature remains neutral with regard to jurisdictional claims in published maps and institutional affiliations.



**Open Access** This article is licensed under a Creative Commons Attribution 4.0 International

License, which permits use, sharing, adaptation, distribution and reproduction in any medium or format, as long as you give appropriate credit to the original author(s) and the source, provide a link to the Creative Commons licence, and indicate if changes were made. The images or other third party material in this article are included in the article's Creative Commons licence, unless indicated otherwise in a credit line to the material. If material is not included in the article's Creative Commons licence and your intended use is not permitted by statutory regulation or exceeds the permitted use, you will need to obtain permission directly from the copyright holder. To view a copy of this licence, visit <http://creativecommons.org/licenses/by/4.0/>.

© The Author(s) 2024